

# Slippery Liquid Infused Porous TiO<sub>2</sub>/SnO<sub>2</sub> Nanocomposite Thin Films via Aerosol Assisted Chemical Vapour Deposition with Anti-Icing and Fog Retardant Properties

Frances L. Heale,<sup>1</sup> Ivan P. Parkin<sup>1</sup> and Claire J. Carmalt<sup>1\*</sup>

<sup>1</sup>Department of Chemistry, University College London, 20 Gordon Street, London, WC1H 0AJ.

## Abstract

Exceptional anti-icing and anti-fogging devices have been synthesised through combination of micro- and/or nano-scale hierarchical thin films followed by a modification with a surface lubricant. Aerosol assisted chemical vapour deposition (AACVD) of single source titanium and tin precursors generated titanium dioxide (TiO<sub>2</sub>)/tin dioxide (SnO<sub>2</sub>) composite thin films. Variation in solvent type and/or combination notably impacted on the resulting intricate surface morphologies, which, upon Krytox lubricant modification, generated slippery liquid infused porous surfaces (SLIPS). The surface topography had a profound effect on the degree of surface ice and fog accumulation. The highest functioning films comprised of hybrid spherical/flowery surface structures generated using a mixed ethyl acetate/dichloromethane solvent system. These films retarded ice formation for >30 min at -10 °C and maintained a high level of sample transparency upon suspension above a heated water bath.

**Keywords:** thin films, SLIPS, anti-icing, anti-fogging, TiO<sub>2</sub>/SnO<sub>2</sub>, nanocomposites, AACVD.

\*Corresponding Author at: Department of Chemistry, University College London, 20 Gordon Street, London, WC1H 0AJ. United Kingdom. Tel: +44 20 7679 7528. E-mail address: [c.j.carmalt@ucl.ac.uk](mailto:c.j.carmalt@ucl.ac.uk) (C. J. Carmalt).

## 1. Introduction

The advancement of modern civilisation relies upon the successful design and manufacture of special wettability materials capable of withstanding environmental challenges.<sup>1</sup> Water repellent ‘smart’ materials<sup>2</sup> are currently central to a plethora of novel applications involving microfluidics,<sup>3</sup> oil-water separation,<sup>4</sup> self-cleaning surfaces<sup>4,5</sup> and anti-icing/-fogging mechanisms.<sup>6,7</sup> Extreme liquid-surface interactions often underpin these technologies and provide favourable alternatives to many energy intensive routes employed to achieve the efficient working and preservation of commercial devices, infrastructure and alike.

Ice accretion is currently a matter of concern for regions of colder climate; the transportation,<sup>8</sup> construction and renewable energy<sup>9-11</sup> sectors face serious economic threats and hazardous operational conditions due to ice accretion and relentless freeze-thaw cycles. The aviation industry has been suffering the consequences of icing events since the 1940s and 1950s because during flight, supercooled water droplets impinge and then freeze on unheated/untreated areas of the aircraft body on which they impact. Aerodynamic performance is therefore substantially compromised due to increased drag and reduced lift.<sup>8</sup> Renewable energy plants, notably wind farms, experience similar setbacks. Light icing increases surface roughness of turbine blades and leads to increased drag, reduced aerodynamic efficiency and a diminished power output.<sup>9-11</sup> Alternatively, material fogging is a serious concern in humid atmospheric conditions. Condensation build-up substantially impacts a material's optical performance, which is problematic for many industrial and domestic applications.<sup>12</sup> Severe personal injury has resulted from fogging of vehicle and aircraft windscreens, with many difficulties stemming from situations where high levels of light transmission are preserved whilst the image is completely distorted.<sup>13</sup>

Several material design strategies have been developed to overcome the setbacks associated with both icing and fogging events. Superhydrophobic surfaces, with water contact angle  $>150^\circ$ , have been thought of as the ideal candidate for ice accretion reduction due to their accentuated wetting behaviour. Ice nucleation is prevented by minimising the liquid-surface interaction time via droplet shedding and/or delayed through a combination of tuned surface roughness and energy.<sup>14,15</sup> Oppositely, many fog prevention films operate on the premise of water sheeting, with water contact angles  $<5^\circ$  (superhydrophilic surface). The surface bound fog, which develops when water condenses onto a surface because of temporary changes in humidity, temperature or convection, fully wets a given material to afford a near-continuous liquid film that mitigates light scattering and preserves optical transmission.<sup>16</sup>

Previous research highlights many of the advantages and limitations associated with the use of smooth, textured or slippery surfaces for targeted ice and fog evasion. Initial attempts to minimise ice adhesion were centred upon low surface energy smooth surfaces. Unstructured polydimethylsiloxane (PDMS) and polytetrafluorethylene (PTFE) samples with contact angles of  $120^\circ$  were proven effective ice-phobes in a study contrasting a variety of smooth surface coatings.<sup>16,18</sup> Peng and Petrenko coated gold and platinum metals with organic compounds that were either strongly hydrophilic or hydrophobic. The contribution of hydrogen bonding to ice adhesion was investigated by varying the degree of hydrophilicity/hydrophobicity in self-assembled monolayers. The smooth monolayer consisted of similar length molecules with the only difference being their outermost groups; recorded ice adhesion properties could therefore be accurately correlated with surface wettability. They determined that the sheer strength of ice was increased with the amount of surface hydrogen bonding; this was further linked to high surface-water affinity.<sup>19</sup> In other work, Wang used the PDMS polymer, Sylgard 184, to determine the effect of coating thickness on ice adhesion strength at  $-10^\circ\text{C}$ . Peak removal stress decreased by a factor of 4 (457 to 115 kPa) with a coating thickness increase from 18 to 533  $\mu\text{m}$ .<sup>20</sup> Smooth anti-fogging surfaces have been generated in Lai's research group using switchable superhydrophilic  $\text{TiO}_2$  films. Stable titanate nanobelt particle suspensions were produced with a pre-hydrolysed surface fluoroalkylsilane coating. Electrophoretic deposition on a conducting glass substrate originally produced a transparent cross-aligned superhydrophobic film. When heated to  $500^\circ\text{C}$  the titanate nanobelt transformed into a porous  $\text{TiO}_2(\text{B})$  film and displayed superhydrophilic characteristics; water on this surface immediately

spread and shed giving it excellent anti-fogging properties.<sup>6</sup> Perfluorinated polyethylene glycol oligomers have also been covalently grafted to silica substrates which were first modified with a reactive isocyanate-silane. The resulting surfaces were oil-hating/water-loving and had improved robustness due to the resistance of covalent linkages to contaminants and solvents; a crucial advancement as many other high energy hydrophilic surfaces were ruined when contaminated with natural oils and airborne organic compounds.<sup>16</sup>

Textured FeCl<sub>3</sub> and HCl etched aluminium alloys with lauric acid modifications were found to postpone icing from 406 s to 787 s, when comparing unmodified with modified substrates at -6 °C, droplet bouncing was also visualised on these microstructured surfaces when sprayed with water at -8 °C.<sup>21</sup> Hydrophobic, water contact angle in the range of 90-150°, and superhydrophobic samples with a coating comprising of nanoparticles embedded in fluorinated polymers were subjected to large supercooled water droplet ice accretion tests. The high surface area samples comprising micro- and nano-scale roughening particles had the lowest wetting hysteresis; ice adhesion strength was recorded as 5.7 times lower than on unstructured alternatives.<sup>22</sup> Unfortunately, the complex structuring associated with these extreme wettability surfaces introduce vulnerabilities. Protrusions and voids between asperities were fragile and experienced degradation within relatively short time frames.<sup>23</sup> Surface roughness incorporation has also had profound effects on anti-fogging functionality. For example, superhydrophobic surfaces prepared via HCl etching of aluminium substrates followed by modification with lauric acid generated superior wetting characteristics. Anti-fogging tests were conducted by placing coated and uncoated substrates into a refrigerator for 5 h before storing in ambient conditions. Within a few minutes, water from the air immediately collected on the bare aluminium substrates; an absence of condensate on the functional sample ensured preservation of optical properties.<sup>24</sup> Despite the many advantageous properties of these textured surfaces, concerns surrounding lifespan and mechanical robustness support the development of alternative 'smart' surfaces models.

Latest developments in the field have centred around slippery liquid infused porous surfaces (SLIPS). SLIPS coatings suppress ice accretion by eliminating moisture from an inert continuous slippery film prior to ice nucleation. A closed-cell architecture is not only thought to eradicate ice accretion but could also maximise mechanical robustness to promote mechanical stability. The lubricant impregnation of structured surfaces is also known to dramatically reduce ice adhesion strengths, 10-150 kPa.<sup>25</sup> In many cases these surfaces fall in the upper threshold for self-removal of accreted ice via wind or natural vibrations, <20 kPa.<sup>7,25</sup> Subramanyam's work indicated that ice adhesion was dependent on the level of surface lubrication as increased accretion was linked to lubricant depletion below the maximum height of surface structures. Ice adhesion was prevented due to lubricant retention within closely spaced structure voids heightening the Laplace pressure.<sup>26,27</sup> Examples of slippery surface for anti-fogging applications have been under-researched even though many of the advantages to their use as icephobes may still apply. Poor longevity made textured materials an ineffective choice in extreme weather conditions and thus initiated investigation into highly specific SLIPS. Aqueous layer on anti-fogging surfaces are expected to solve lifespan issues through lubricant replenishment from environmental moisture; innate hydrophilicities should afford droplet spreading and, more critically, maintain optical properties.

Highly textured titanium dioxide (TiO<sub>2</sub>)-tin dioxide (SnO<sub>2</sub>) nanocomposites have been previously generated for their use as photocatalysts. Chadwick et al. made use of combinatorial aerosol assisted chemical vapour deposition (cAACVD) to produce mix phase films with monolithic surface morphologies.<sup>29,30</sup> These robust films had many of the qualities desired of anti-icing/-fogging materials; an innate water repellency and high surface area nano-oxide features provided adequate incentive to explore alternative functionalities.<sup>28,29</sup>

Here we present the use of AACVD to generate mixed morphology TiO<sub>2</sub>-SnO<sub>2</sub> films with further SLIPS modification. Varying solvent systems afforded unique surface features, which impacted the way in which the spin coated lubricant interacted with the film surface. Since it has been understood that liquid repulsion alone does not guarantee anti-icing or -fogging characteristics, SLIPS provide an extra dimension and are now revolutionising the way in which the potential impacts of harsh environmental conditions are managed. The TiO<sub>2</sub>-SnO<sub>2</sub> SLIPS surfaces described are multifunctional showing unique ice and fog retarding properties.

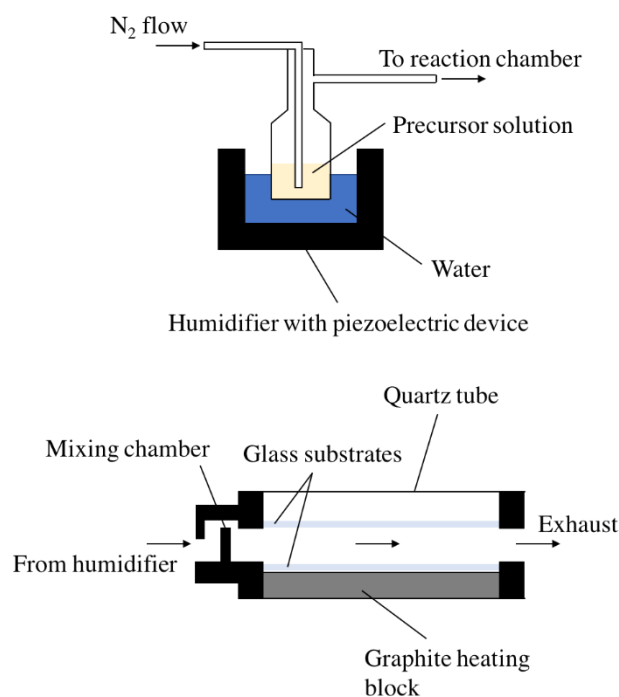
## 2. Experimental

### 2.1. Materials

Nitrogen (99.99%) was supplied from BOC and SiO<sub>2</sub> coated float-glass was supplied from Pilkington NSG. The solvents, ethyl acetate (99%), toluene (99%) and dichloromethane (99%), were obtained from Fischer Scientific and the precursors, titanium isopropoxide (99%) and butyltin trichloride (99%), were obtained from Sigma-Aldrich. Krytox lubricant was purchased from Dow Corning. All chemicals were of analytical standard and used as received.

### 2.2. AACVD of titanium isopropoxide and butyltin trichloride

A range of surface textures were generated via AACVD of titanium isopropoxide and butyltin trichloride precursors. Thin films were produced on SiO<sub>2</sub> barrier coated float-glass using a cold wall CVD reactor, **Figure 1**.



**Figure 1.** Aerosol assisted chemical vapour deposition (AACVD) apparatus.

Prior to use, glass substrates (90 mm x 45 mm x 4 mm) were cleaned with isopropanol followed by acetone and then air dried. Inside the reactor, a graphite block containing a Whatman cartridge heater was used to heat the glass substrate to 450 °C and the temperature was monitored with a PtRh thermocouple. Precursors were dissolved in the desired solvent combination and vaporised at room temperature using a PIFCO ultrasonic humidifier, **Table 1**. The resulting aerosol was carried into the reactor in a stream of nitrogen gas (1.0 Lmin<sup>-1</sup>) through a brass baffle to achieve laminar flow. Deposition completion times varied, 25-35 min, based on precursor and solvent combination but upon completion the coated glass substrate was cooled to <100 °C, under nitrogen flow before removal.

**Table 1.** Surface structure generation via aerosol assisted chemical vapour deposition (AACVD) for anti-icing and anti-fogging applications.

Sample	AACVD solution				
	Titanium isopropoxide/g	Butyltin trichloride/g	Ethyl acetate/ml	Toluene/ml	Dichloromethane/ml
1	0.50	0.50	15	15	0
2	0.50	0.50	0	30	0
3	0.50	0.50	30	0	0
4	0.50	0.50	0	0	30
5	0.50	0.50	0	15	15
6	0.50	0.50	15	0	15

### 2.3. Fabrication of slippery liquid infused porous surfaces (SLIPS)

Glass films, generated from the precursor solutions in **Table 1**, were cut into small coupons (100 mm x 10 mm x 4 mm) and spin coated with Krytox ( $0.5 \text{ cm}^{-3}$ ) for 30 s at 2000 rpm. Lubricated samples were stored at room temperature without disrupting the now optimised anti-icing and anti-fogging surface layers.

### 2.4. Characterisation

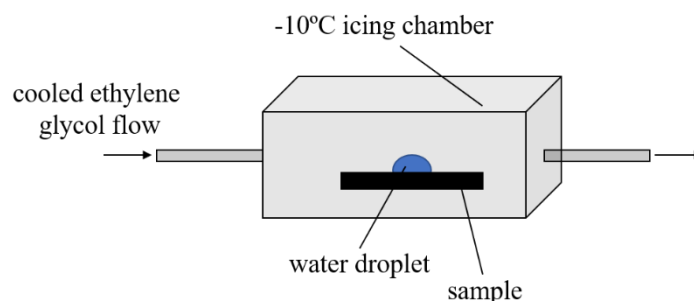
X-ray photoelectron spectroscopy (XPS) was carried out using a thermo Scientific X-ray photoelectron spectrometer with a monochromated Al- $K_{\alpha}$  X-ray source ( $8.3381 \text{ \AA}$ ). Peaks were modelled using CasaXPS software and binding energies were adjusted for adventitious carbon ( $284.5 \text{ eV}$ ). X-ray diffraction (XRD) patterns were obtained using a Bruker D8 Discover diffractometer with monochromated Cu- $K_{\alpha}$  radiation ( $1.5406 \text{ \AA}$ ). Raman spectra were recorded between  $100$  and  $1200 \text{ cm}^{-2}$  on a Reinshaw 1000 spectrometer equipped with a  $514.5 \text{ nm}$  laser. Surface topographies were investigated using a JEOL JSM-6301F scanning electron microscope (SEM) with an acceleration voltage of  $5$  or  $10 \text{ kV}$ ; films were gold coated prior to SEM analysis to negate charging effects. Atomic force microscopy (AFM) was completed on a Bruker Dimension Icon instrument to 3D map sample surfaces. Ultraviolet-visible (UV-Vis) spectroscopy was carried out on a Shimadzu UV-2700 spectrophotometer in transmission mode between the wavelengths of  $250$  and  $900 \text{ nm}$ .

### 2.5. Functionality and performance testing

Three static water contact angles were measured per coating at ambient temperature via the sessile-drop method using an FTA 100 optical contact angle meter ( $13.00 \mu\text{g}$  water droplet). The average value and associated error were calculated for each sample. The tilting/sliding angle, defined as the angle at which a water droplet readily slides off a slanted surface (fixed droplet weight of  $0.5000 \text{ g}$ ), was recorded using a digital angle finder. Averages and standard deviations were calculated.

Anti-icing performance was accurately monitored using the testing set-up outlined in **Figure 2**. Samples ( $10 \text{ mm} \times 10 \text{ mm} \times 4 \text{ mm}$ ) were placed in a sealed cooling chamber ( $10 \text{ cm} \times 10 \text{ cm} \times 5 \text{ cm}$ ) held at  $-10 \text{ }^{\circ}\text{C}$ . The appropriate temperature was achieved via a through flow of cooled ethylene glycol and monitored using a PtRh thermocouple. A water droplet ( $0.0088 \text{ g}$ ) was immediately placed on the sample surface and droplet freezing time was recorded. Averages and standard deviations were calculated based on three repeat results per sample. Freeze-thaw cycle testing involved removing the iced droplet covered sample from the chamber, allowing it to thaw, placing it back in icing apparatus and recording the time taken to the next icing event. Additional qualitative anti-frosting testing was carried out with liquid nitrogen. Samples were submerged in the cryogenic fluid for  $1 \text{ min}$  and then left to stand at room temperature and humidity for a further  $1 \text{ min}$ . Sample transparency was promptly assessed using images.

The samples' anti-fogging ability was determined by holding sample coupons (10 mm x 10 mm x 4 mm) 10 cm above an 80 °C water bath for 1 min. Images and ultraviolet-visible spectra were collected after acclimatisation to room temperature and pressure, for 1 min.



**Figure 2.** Anti-icing testing apparatus. Samples were placed into a -10 °C chamber and time taken for water droplet, 0.008 g, freezing was recorded.

### 3. Results and Discussion

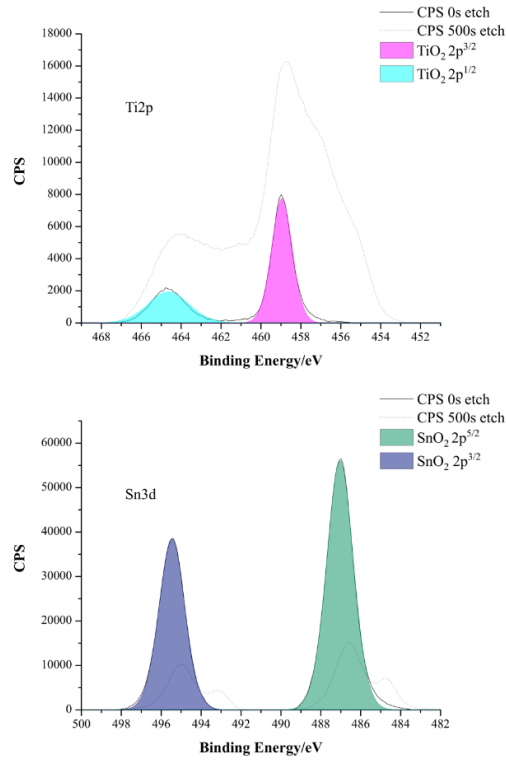
AACVD of titanium isopropoxide and butyltin trichloride resulted in the formation of composite thin films that were modified with a Krytox lubricant. The highly functional slippery liquid infused porous surfaces (SLIPS) effectively prevented ice and fog accretion through combination of micro- and nano-scale topographies with a surface lubricant top layer. Surfaces were characterised and functionally tested as follows.

#### 3.1 Characterisation

X-ray photoelectron spectroscopy (XPS) data was used to determine the oxidation state of the elements present in the titanium dioxide (TiO<sub>2</sub>)-tin dioxide (SnO<sub>2</sub>) thin films, **Figure 3**. In film sample **6**, Ti2p<sup>3/2</sup> had a binding energy of 458.9 eV which corresponded to Ti<sup>4+</sup>; the binding energy of Sn3d<sup>3/2</sup> was 486.9 eV and corresponded to Sn<sup>4+</sup>.<sup>34</sup> Elemental abundance at the film surface and in the bulk were calculated by comparing the area under the various peaks in their respective scans, as shown in **Table 2**. It was found that the surface was 2.6 times richer in SnO<sub>2</sub> compared with TiO<sub>2</sub>. The reverse was true of the bulk, which was 6.2 times richer in TiO<sub>2</sub> and SnO<sub>2</sub>. This film growth pattern was characteristic of similar depositions outlined in the literature where films consistently contained more Ti than Sn.<sup>29</sup> The trend was characteristic of all thin film samples made in this study.

The X-ray diffraction (XRD) patterns of thin film samples **1-6**, **Table 1**, are represented in **Figure 4**. Anatase TiO<sub>2</sub> peaks were clearly identified in the composite films at 25° (101), 37° (112), 54° (105) and 55° (211). The cassiterite SnO<sub>2</sub> crystal structure was characterised from peaks at 27° (110) and 34° (101). Preferential growth in these noted planes proved that the presence of two oxides had an impact on crystal orientation. This assumption was supported

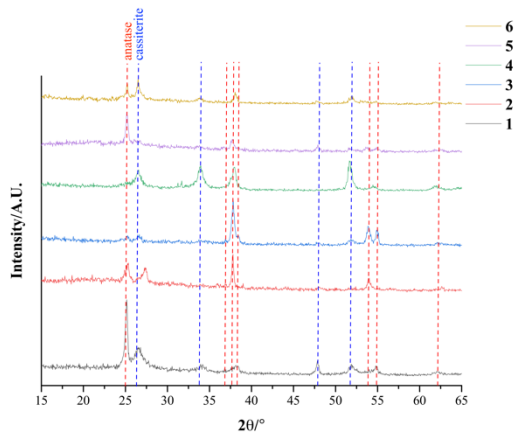
by the clear difference in preferred orientation between pure  $\text{TiO}_2$  and  $\text{SnO}_2$  films documented in the literature/ICSD and these composite films.<sup>29</sup>



**Figure 3.** X-ray photoelectron spectroscopy (XPS)  $\text{Ti}2p$  and  $\text{Sn}3d$  scans for thin film sample **6**, precursor solution composition outlined in **Table 1**. 0s and 500s etch scans represent surface and bulk material.

**Table 2.** Change in atomic abundance with etch time for film sample **6**, precursor solution composition outlined in **Table 1**. Derived from X-ray photoelectron spectroscopy (XPS).

Etch time/s	Atomic abundance/%							
	C		O		Ti		Sn	
	Value	Error	Value	Error	Value	Error	Value	Error
0	38.3	3.8	43.1	4.3	4.4	0.4	14.2	1.4
500	3.2	0.3	64.2	6.4	27.2	2.7	5.4	0.5



**Figure 4.** X-ray diffraction (XRD) patterns for thin film samples **1-6**, precursor solution composition outlined in **Table 1**. Anatase and cassiterite peaks have been denoted with red and blue vertical dotted lines respectively.



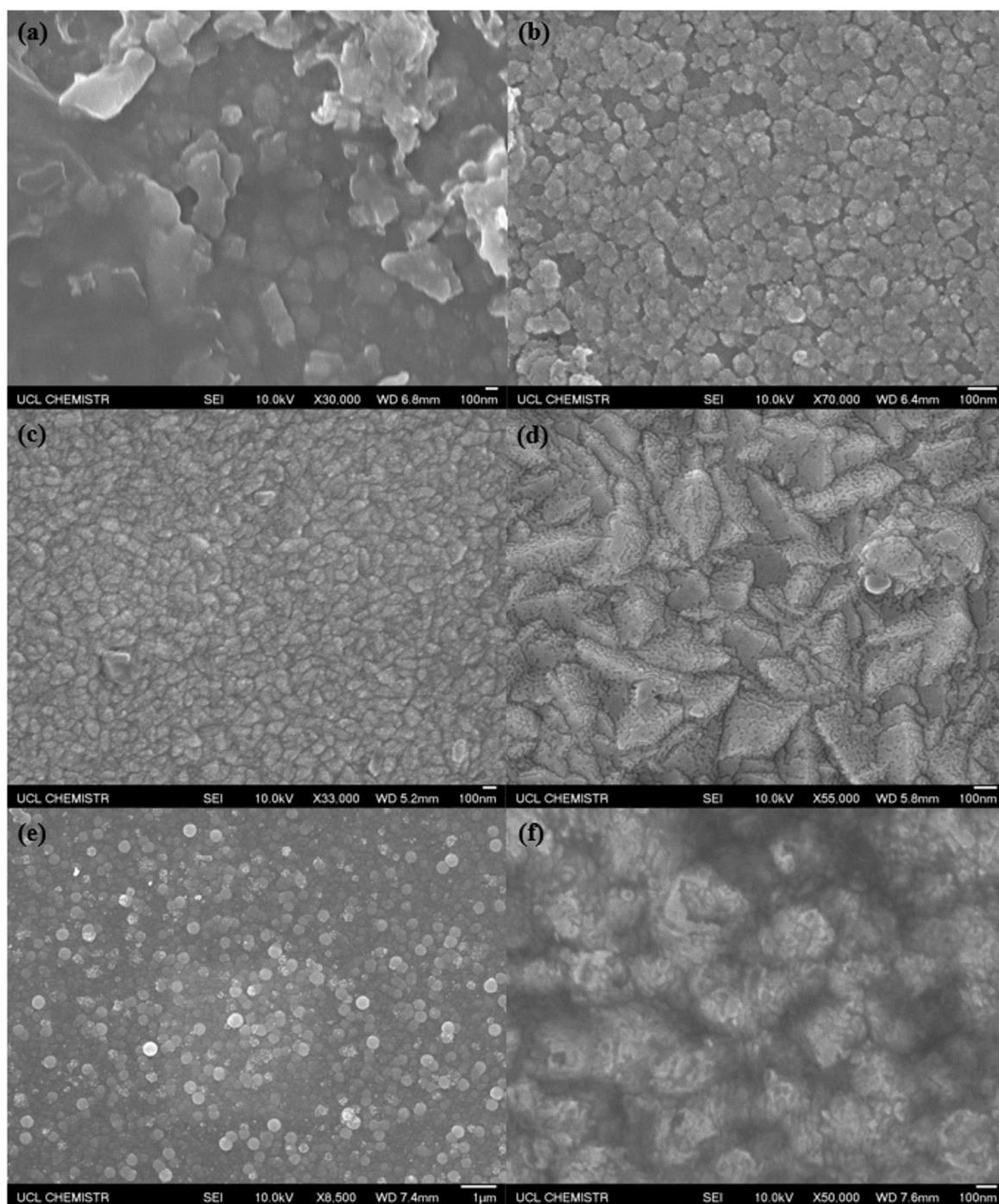
There was no evidence of the expected TiO<sub>2</sub> anatase or SnO<sub>2</sub> peaks in the Raman spectra of thin film samples **1-5**; a suspected result of film thickness or surface carbon contaminants. However, the spectrum recorded for sample **6** showed peaks that were assigned to TiO<sub>2</sub> anatase tetragonal symmetry.<sup>29</sup> The E<sub>g</sub> peak was seen at 145 cm<sup>-1</sup> and matched closely with that of a pure TiO<sub>2</sub>, which indicated there was little impact on unit cell size upon composite formation.<sup>29</sup>

Scanning electron microscope (SEM) images of thin film samples **1-6** clearly highlighted the effects of varying solvent composition in the precursor solutions, **Figure 5**. Ti and Sn precursors were consistently included in equal molar quantities; the solvent variation/combination was solely responsible for morphological changes. Surface topography was closely linked to anti-icing -fogging performance so a better understanding of its impact was desired. The three solvent properties thought to have the greatest effect on film topography are dielectric constant, viscosity and volatility, **Table 3**. The relatively small difference in toluene, ethyl acetate and dichloromethane's dielectric constants supports the good miscibility visualised when combining solvents as well as when incorporating Sn and Ti sources. Solvent viscosities are also of the same order of magnitude and were therefore not expected to play a hugely significant role in film growth rate or surface feature size. It was therefore concluded that solvent volatility was responsible for the changes in film uniformity and size of surface structures; higher volatility was correlated to enhanced rate of precursor delivery to the substrate surface. Dichloromethane had the lowest boiling point of all solvents used in AACVD reactions, 40 °C, and toluene the largest, 111 °C. Consequently, films made using dichloromethane had some of the largest, most uniform and close packed surface features that protruded furthest from the substrate plane. This was confirmed using SEM and AFM, **Figure 5** and **6**. The opposite was true of films generated using toluene. Samples **3**, **4** and **6** were made from precursor solutions that did not include toluene, the afforded films had the longest average time to water droplet freezing and were therefore more functional, described in section 3.2.<sup>30-32</sup>

**Table 3.** Dielectric constant, viscosity and boiling point values for toluene, ethyl acetate and dichloromethane.<sup>30</sup>

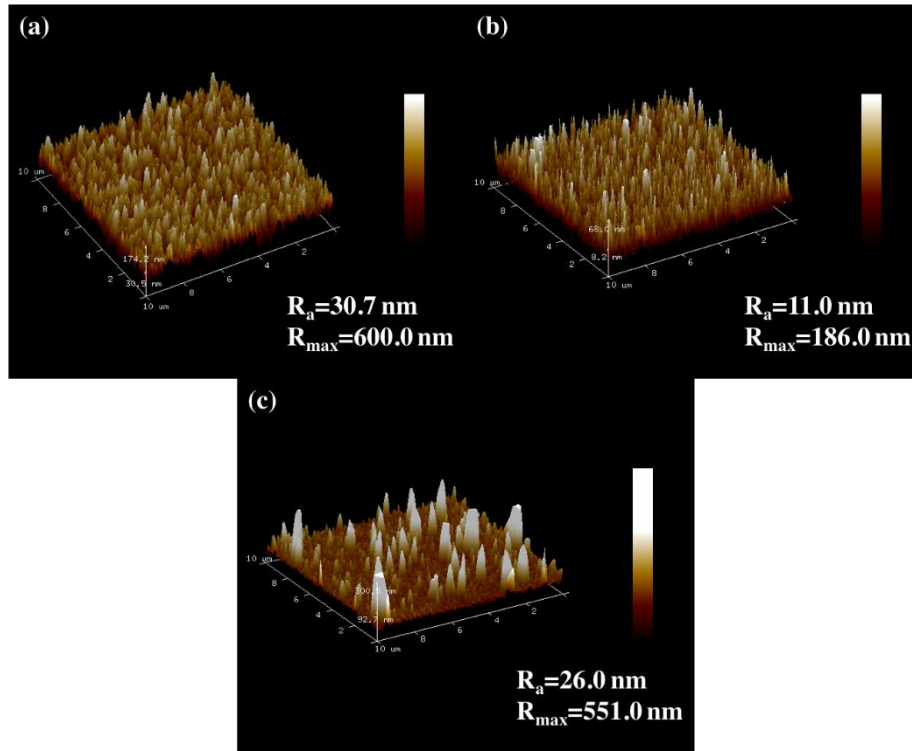
Solvent	Dielectric constant	Viscosity x10 <sup>-3</sup> /Pa.s	Boiling point/°C
Toluene	2.38	0.552	111
Ethyl acetate	6.02	0.426	77
Dichloromethane	8.93	0.830	40

Film **1**, generated from an ethyl acetate/toluene solvent system, had non-uniform surface protrusions that had no clearly identifiable shape; many particle clusters were larger than 1 μm. Toluene was used to produce film **2**'s planar flowered structure, around 100 nm in diameter, while ethyl acetate created film **3**'s needle/sphere hybrid morphology. Dichloromethane afforded the well-defined and uniform 200 nm needles of film **4**. Film **5** comprised of perfectly spherical particles which were highly uniform and evenly distributed; a product of a toluene/dichloromethane solvent system. Finally, film **6**'s risen flower structure was a result of an ethyl acetate and dichloromethane solvent precursor mixture. This film displayed intricately textured nanoparticles, 150 nm in diameter, that had 90% surface coverage. It was this multi-scale 'structure upon structure' that increased the film's surface area. Higher densities of jagged protrusions and film pores ultimately lead to a delay in ice nucleation.



**Figure 5.** Scanning electron microscope (SEM) images (a)-(f) correspond to thin film samples 1-6, precursor solution composition outlined in **Table 1**. Samples were gold coated prior to analysis to reduce charging effects.

Atomic force microscopy (AFM) gave an insight into the films' 3D surface features and average roughness values, **Figure 6**. Thin films generated from a Ti/Sn precursor solution containing either toluene, ethyl acetate or dichloromethane corresponded to samples **2-4** respectively. The toluene solvent system saw film protrusions in the vertical plane averaging 30.7 nm, the smallest 11.0 nm structures were a product of the ethyl acetate solvent and needle features protruding from the surface by 26.0 nm were characteristic of dichloromethane-based systems. Unfortunately, it was not possible to get useful AFM analysis for samples **1** and **6** due to the films' more extreme micro-cluster roughness.



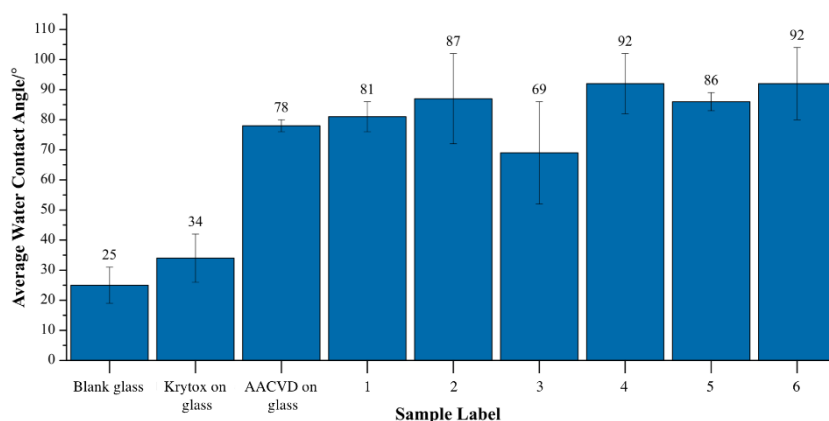
**Figure 6.** Atomic force microscope (AFM) images (a)-(c) correspond to thin film samples **2-4**, precursor solution composition outlined in **Table 1**. Average roughness ( $R_a$ ) and maximum roughness ( $R_{max}$ ) factors have been quoted.

### 3.2 Coating Functionality and Performance

Film coating samples were spin coated with Krytox lubricant to afford slippery liquid infused porous surfaces (SLIPS), **Figure 5**. Sample functionality and performance included evaluation of the average water contact and tilting angles, time to surface water droplet freezing in sub-zero conditions, degree of surface frosting after emersion in liquid nitrogen and degree of fogging after sample suspension above an 80 °C water bath.

Average water contact angles were recorded on blank glass, Krytox coated on blank glass, non-SLIPS thin film sample **1**, with samples **2-6** falling within experimental error, and SLIPS thin film samples **1-6**. Results are shown in **Figure 7** and precursor solutions for all AACVD experiments were outlined in **Table 1**. Average water contact angles on blank glass and Krytox on glass samples were  $25 \pm 6^\circ$  and  $4 \pm 8^\circ$  respectively, whilst a value of  $78 \pm 8^\circ$  was recorded

on non-SLIP thin film sample **1**. Thin film SLIPS samples **1-6** did not show any further substantial increase in water repellency so it was possible to deduce that water contact angle was only dependent on the presence of surface structure. Water tilting angle measurements displayed the opposite trend. Complete droplet adhesion was visualised on blank glass and non-SLIPS thin film sample **1**, whereas water tilting angles were  $<5^\circ$  on all lubricant coated surfaces.

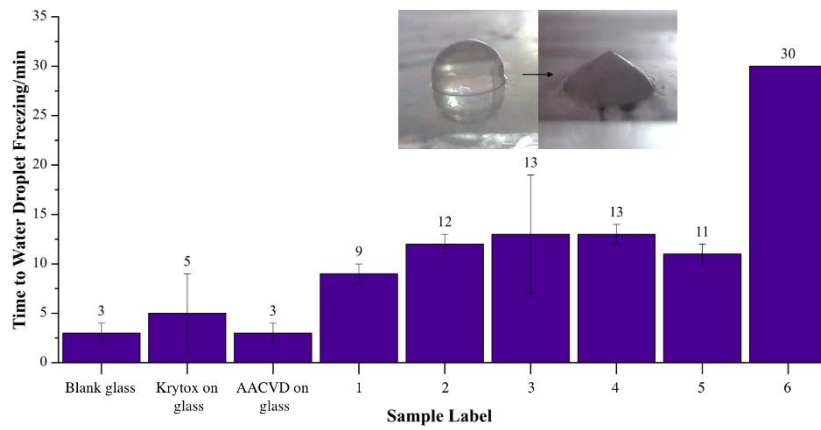


**Figure 7.** Average water contact angle results for blank glass, Krytox on glass, non-SLIPS thin film sample and SLIPS thin film samples **1-6**, precursor solution composition outlined in **Table 1**.


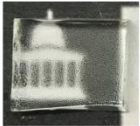




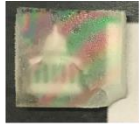

Sealed in a  $-10^\circ\text{C}$  chamber, water droplets were placed on a standard, a smooth SLIPS surface, a non-SLIPS thin film and SLIPS thin film samples **1-6**. Time taken for the respective water droplets to freeze was determined as a measure of anti-icing capability, **Figure 8**. Droplets on blank glass and the non-SLIPS textured thin film sample froze in the shortest time period,  $3\pm 1$  min. The Krytox on glass standard was able to delay freezing for  $5\pm 4$  min and therefore highlighted the potential benefit of SLIPS for anti-icing applications. SLIPS thin film samples **1-6** were consequently tested in a similar fashion. Sample **1** delayed ice formation by  $9\pm 1$  min and proved that surface structures in combination with surface lubricant beneficially affected icing results. Samples **2-5** displayed further enhanced icephobicities – a direct result of varying surface topographies. The thin film generated using a dichloromethane solvent system prior to lubricant coating, sample **4**, retarded ice formation for  $13\pm 1$  min. Unlike sample **1**, this hydrophobic film had a uniform nano-needle topography that protruded a greater distance out of the film's horizontal plane,  $R_{\text{max}}=551.0$  nm. Sample **6** outperformed all other surfaces by consistently preventing ice accretion for  $>30$  min. This uniform surface appeared to have hybrid micro and nano-sphere/-flower structures and was deposited using an ethyl acetate/dichloromethane solvent system prior to lubricant modification. Functional testing results supported the theory that a combination of surface roughness and lubrication provided unique benefits that neither physical characteristic alone could provide. The surface of sample **6** was able to delay icing for  $>25$  mins longer than the separate lubricant or corresponding thin film sample standards. Exceptional film durability was realised after running a scalpel up and down the length of all SLIPS samples ten times. Initial scalpel markings were seen in the Krytox surface layer, which spontaneously refilled with surrounding lubricant after  $\sim 3$  s. This regeneration left the films' functionality unchanged within the original experimental error. It was also noted that functionality was preserved within experimental error upon leaving films open to the atmosphere for 50 days providing that the lubricant wasn't removed with fabric or

alike via a wiping action. The final durability result was collected using sample **6**. The coating was initially placed in  $-10\text{ }^{\circ}\text{C}$  conditions and the time taken for a surface water droplet ( $0.0088\text{ g}$ ) to freeze was recorded. The sample was then immediately exposed to room temperature and pressure and was left in said conditions until the non-transparent solid droplet melted. A further 24 identical freeze-thaw cycles saw no alteration to the  $>30\text{ min}$  droplet freezing time and supported previous film stability findings. Unfortunately, the absence of a standardised ice accretion test made literature comparison a non-trivial prospect. Superhydrophobic nanostructured silicon substrates described by Alizadeh et al. Materials in this publication were able to delay the freezing of a  $4\text{ }\mu\text{L}$  DI water droplet by  $60\text{ s}$  after acclimatisation to  $-20\text{ }^{\circ}\text{C}$  conditions.<sup>33</sup> Many other papers cite the ice adhesion strength on samples but neglect to quote freezing temperatures or time to freezing. Ice adhesion values of  $25\text{ kPa}$  at temperatures down to  $-53\text{ }^{\circ}\text{C}$  have been recorded on comparable SLIPS, even after 30 icing-de-icing cycles.<sup>25</sup>

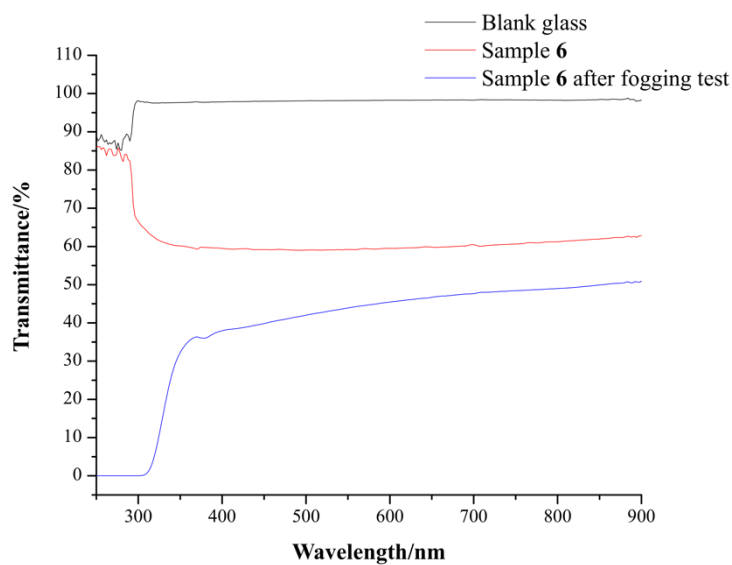
Identical samples were then tested for anti-frosting characteristics. They were first submerged in liquid nitrogen, for  $1\text{ min}$ , and then left to stand at room temperature and humidity, for  $1\text{ min}$ . Frost formation was visually monitored via transparency assessment, **Figure 9**. Anti-fogging properties were tested by holding sample coupons, slippery side down,  $10\text{ cm}$  above  $80\text{ }^{\circ}\text{C}$  water for  $1\text{ min}$ . The degree of fogging/visual obstruction was recorded after  $1\text{ min}$  of acclimatisation to room temperature and humidity, **Figure 9**. Blank glass standards performed poorly in both frosting and fogging tests; visual performance was entirely and partially compromised in the case of the frosting and fogging experiments respectively. The Krytox coated glass sample permitted a significant amount of ice adhesion but prevented collection of condensed water vapour whereas the non-SLIPS thin films saw excessive frost and fog accumulation. SLIPS thin film samples were determined the most effective frost-phobic and fog-phobic materials. **Figure 10** displays the ultraviolet-visible (UV-Vis) spectra of sample **6** before and after the fogging test, as described above. The blank glass standard had between  $95\%$  and  $100\%$  transmittance in the visible region, which was reduced to  $\sim 60\%$  upon functionalisation via thin film deposition and spin coating with a lubricant layer. More importantly, fogging tests only slightly reduced the sample's transparency,  $\sim 50\%$ , therefore supporting the qualitative evidence that visual performance wasn't greatly compromised. The surface structure/lubricant combination substantially retarded foreign material adhesion as the oily surface layer could effectively saturate film pores thus reducing the number of ice nucleation sites and promoting condensate sheeting. After consideration of the qualitative and ambiguous nature of functional testing, coatings fabricated in this study prevented build-up of frost and/or fog to a similar degree as those documented in the literature.<sup>16,35-37</sup>



**Figure 8.** Icing results for blank glass, Krytox on glass, non-SLIPS thin film sample and SLIPS thin film samples 1-6, precursor solution composition outlined in **Table 1**. Time to water droplet icing upon samples in  $-10\text{ }^{\circ}\text{C}$  conditions were recorded.

Sample	Frosting test	Fogging test
Blank glass		
Krytox on glass		
Non-SLIPS sample 6		
SLIPS sample 6		

**Figure 9.** Frosting and fogging qualitative test images for blank glass, Krytox on glass, non-SLIPS thin film sample 6. Precursor solution compositions outlined in **Table 1**. Frosting experiments were carried out by submerging sample coupons in liquid nitrogen whilst fogging tests were performed above an 80 °C water bath for 1 min. Images were collected after acclimatisation to room temperature and pressure, for 1 min.



**Figure 10.** Ultraviolet-visible spectroscopy of blank glass and SLIPS thin film sample 6 before and after the fogging test. Fogging tests were performed by holding samples above an 80 °C water bath for 1 min. Data was collected after acclimatisation to room temperature and pressure, for 1 min.

## 4. Conclusion

Titanium dioxide (TiO<sub>2</sub>)-tin dioxide (SnO<sub>2</sub>) thin film composites were made via aerosol assisted chemical vapour deposition (AACVD) prior to spin coating with a Krytox lubricant. The afforded slippery liquid infused porous surfaces (SLIPS) has underlying intricate nano-/micro-scale textures and therefore displayed exceptional anti-icing and anti-fogging functionalities.

The AACVD of titanium isopropoxide and butyltin trichloride precursors dissolved in an ethyl acetate/dichloromethane solvent system afforded a uniform thin film with hybrid nano-sphere/-flower protrusions. Upon spin coating with a lubricant, said hydrophobic samples consistently retarded ice accretion for >30 min in -10 °C conditions and maintained reasonable levels of optical transparency after frosting and fogging testing. The uniform nano-flower structures outperformed other surface features, such as nano-spheres/-needles and micro textures, generated using alternative AACVD solvent systems. It was suspected that ice nucleation sites were reduced and water sheeting was maximised (to prevent fogging) due to the uniform network of highly textured nano-scale protrusions in which the lubricant could fully saturate.

## Conflicts of interest

There are no conflicts to declare.

## 5. Acknowledgements

The authors wish to thank Innovate UK (102541), EPSRC for grant EP/N510051 and for studentship funding (FLH) through the M<sup>3</sup>S Doctoral Training Centre (grant EP/G036675) and Akzonobel for financially supporting this project.

## References

- 1 Crick, C.; Parkin I.; Preparation and Characterisation of Super-Hydrophobic Surfaces *Chemistry* 2010, 16, 3568-3588.
- 2 Zhang X.; Shi F.; Niu J.; Jiang Y.; Wang Z.; Superhydrophobic Surfaces: from Structural Control to Functional Application *J. Mat. Chem.* 2008, 18, 621-633.
- 3 Vinogradova O.; Dubov A.; Superhydrophobic Textures for Microfluidics *Mend. Commun.* 2012, 22, 229-236.
- 4 Zhu H.; Chen D.; Li N.; Xu Q.; Li H.; Lu J.; Dual-layer Copper Mesh for Integrated Oil-Water



- Separation and Water Purification Appl. Cat. B: Environ. 2017, 200, 594-600.
- 5 Afzal S.; Daoud W.; Langford S.; Superhydrophobic and Photocatalytic Self-Cleaning Cotton J. Mat. Chem. A 2014, 2, 18005-18011.
  - 6 Lai Y.; Tang Y.; Gong J.; Gong D.; Chi L.; Lin C.; Chen Z.; Transparent Superhydrophobic/Superhydrophilic TiO<sub>2</sub>-Based Coatings for Self-Cleaning and Anti-Fogging J. Mat. Chem. 2012, 22, 7420-7426.
  - 7 Susoff M.; Siegmann K.; Pfaffenroth C.; Hirayama M.; Evaluation of Icephobic Coatings – Screening of Different Coatings and Influence of Roughness Appl. Surf. Sci. 2013, 282, 870-879.
  - 8 Gent R.; Dart N.; Cansdale J.; Aircraft Icing Phil. Trans. R. Soc. Lond. A 2000, 358, 2873-2911.
  - 9 Carriveau R.; Edrisy A.; Cadieux P.; Mailloux R.; Ice Adhesion Issues in Renewable Energy Infrastructure J. Adhes. Sci. Tech. 2012, 26, 447-461.
  - 10 Cucchiella F.; Dadamo I.; Estimation of the Energetic and Environmental Impacts of a Roof-Mounted Building-Integrated Photovoltaic Systems Renew. Sustain. Energy Rev. 2012, 16, 5245-5259.
  - 11 Jelle B.; The Challenge of Removing Snow Downfall on Photovoltaic Solar Cell Roofs in Order to Maximize Solar Energy Efficiency – Resarch Opportunities for the Future Energy Build. 2013, 67, 334-351.
  - 12 Varshney P.; Mohapatra S.; Kumar A.; Fabrication of Mechanically stable Superhydrophobic Aluminium Surface with Excellent Self-Ceaning and Anti-Fogging Properties Biomimetics 2017, 2, 1-12.
  - 13 Lee H.; Alcaraz M.; Rubner M.; Cohen R.; Zwitter-Wettability and Antifogging Coatings with Frost-Resisting Capabilities ACS Nano 2013, 7, 2172–2185.
  - 14 Richard D.; Clanet C.; Quéré D.; Contact Time of a Bouncing Drop Nature, 2002, 417, 811–811.
  - 15 Richard D.; Quéré D.; Bouncing Water Drops Europhys. Lett. 2000, 50, 769–775.
  - 16 Howarter J.; Youngblood J.; Self-Cleaning and Next Generation Anti-Fog Surfaces and Coatings Macromol, Rapid Commun. 2008, 29, 455–466.
  - 17 Jellinek H.; Kachi H.; Kittaka S.; Lee M.; Yokota R.; Ice Releasing Block-Copolymer Coatings Colloid Polym. Sci. 1978, 256, 544–511.
  - 18 Saito H.; Takai K.; Yamauchi G.; Water- and Ice-Repellent Coatings Surf. Coatings Int. 1997, 80, 168–171.
  - 19 Petrenko V.; Peng S.; Reduction of Ice Adhesion to Metal by using Self-Assembling Monolayers (SAMs) Canadian J. Phys. 2003, 81, 387–393.
  - 20 Yorkgitis E.; Melancon K.; Hine A.; Giaquinto S.; Glaciphobic Polymeric Materials J. Adhes. Sci. Tech. 2012, 26, 681–699.
  - 21 MinR.; Wen L.; Baoshan W.; Binwei D.; Fumin M.; Zhanlong Y.; Preparation and Anti-Icing Behaviour of Superhydorphobic Surfaces on Aluminium Alloy Substrates Langmuir 2013, 29, 8482–8491.
  - 22 Kulinich S.; Farzaneh M.; Ice Adhesion on Superhydrophobic Surfaces Appl. Surf. Sci. 2009, 255, 8153–8157.
  - 23 Varanasi K.; Tao D.; Smith D.; Hsu M.; Bhate N.; Frost Formation and Ice Adhesion on Superhydrophobic Surfaces Appl. Phys. Lett. 2010, 97, 2341021–2341023.

- 24 Varshney P.; Lomga J.; Gupta P.; Mohapatra S.; Kumar A.; Durable and Regenerable Superhydrophobic Coatings for Aluminium Surfaces with Excellent Self-cleaning and Anti-Fogging Properties *Tribol. Int.* 2018, 119, 38–44.
- 25 Dou R.; Chen J.; Zhang Y.; Wang X.; Cui D.; Song Y.; Jiang L.; Wang J.; Anti-Icing Coating with an Aqueous Lubricating Layer *ACS Appl. Mat. Int.* 2014, 6, 6998–7003.
- 26 Subramanyam S.; Rykaczewski K.; Varanasi K.; Ice Adhesion on Lubricant-Impregnated Textured Surfaces *Langmuir* 2013, 29, 13414–13418.
- 27 Kim P.; Kreder M.; Alvarenga J.; Aizenberg J.; Hierarchical or Not? Effect of the Length Scale and Hierarchy of the Surface Roughness on Omniphobicity of Lubricant-Infused Substrates *Nano Lett* 2013, 13, 1793–1799.
- 28 Chadwick N.; Sathasivam S.; Kafizas A.; Bawaked S.; Obaid A.; Al-Thabaiti S.; Basahel S.; Parkin I.; Carmalt C.; Combinatorial Aerosol Assisted Chemical Vapour Deposition of a Photocatalytic Mixed SnO<sub>2</sub>/TiO<sub>2</sub> Thin Film *J. Mat. Chem. A* 2014, 2, 5108-5116.
- 29 Ponja S.; Sathasivam S.; Chadwick N.; Kafizas A.; Bawaked S.; Obaid A.; Al-Thabaiti S.; Basahel S.; Parkin I.; Carmalt C.; Aerosol Assisted Chemical Vapour Deposition of Hydrophobic TiO<sub>2</sub>-SnO<sub>2</sub> Composite Film with Novel Mictrostructure and Enhanced Photocatalytic Activity *J. Mat. Chem. A* 2013, 1, 6271-6278.
- 30 Smallwood I.; *Handbook of Organic Solvent Properties* Butterworth-Heinemann 1997, 1st edn.
- 31 Potter D.; Parkin I.; Carmalt C.; The Effect of Solvent on Al-Doped ZnO Thin Films Deposited Via Aerosol Assisted CVD *RSC Adv.* 2018, 8, 33164-33173.
- 32 Wang W.; Purwanto A.; Lenggoro I.; Okuyama K.; Chang H.; Jang H.; Investigation on the Correlations Between Droplet and Particle Size Distribution in Ultrasonic Spray Pyrolysis *Ind. Eng. Chem. Res.* 2008, 47, 1650-1659.
- 33 Alizadeh A.; Masako Y.; Li.; Shang w.; Otta S.; Zhong S.; Ge L.; Dhinojwala A.; Conway K.; Bahadur V.; Vinciguerra J.; Stephens B.; Blohm M.; Dynamics of Ice Nucleation on Water Repellent Surfaces *Langmuir* 2012, 28, 3180–3186.
- 34 Beamson D.; Briggs G.; High Resolution XPS of Organic Polymers: The Scienta ESCA300 Database *J. Chem. Educ.* 1993, 70, 25-318.
- 35 Wang L.; Lu J.; Wang M.; Zhang B.; Hou Y.; Liu G.; Yang W.; Liu J.; Anti-Fogging Performances of Liquid Metal Surface Modified by ZnO Nano-Petals *J. Tai. Inst. Chem. Eng.* 2019, 95, 65-70.
- 36 Lai Y.; Tang Y.; Gong J.; Chi L.; Lin C.; Chen Z.; Transparent Superhydrophobic/Superhydrophilic TiO<sub>2</sub>-Based Coatings for Self-Cleaning and Anti-fogging *J. Mat. Chem.* 2012, 22, 7420-7426.
- 37 Lomga J.; Varshney P.; Nanda D.; Satapathy M.; Mohapatra S.; Kumar A.; Fabrication of Durable and Regenerable Superhydrophobic Coatings with Excellent Self-Cleaning and Anti-Fogging Properties for Aluminium Surfaces *J. Alloys Comp.* 2017, 702, 161-170.